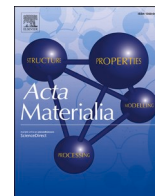| Title	Experimental and first-principles insights into Ti-mediated Cu-Si₃N₄ interfaces for high-reliability electronic substrates
Author(s)	Tatsumi, Hiroaki; Nitta, Shunya; Ito, Atsushi M. et al.
Citation	Acta Materialia. 2025, 304, p. 121813
Version Type	VoR
URL	https://hdl.handle.net/11094/103702
rights	This article is licensed under a Creative Commons Attribution 4.0 International License.
Note	

Full length article

Experimental and first-principles insights into Ti-mediated Cu–Si$_3$N$_4$ interfaces for high-reliability electronic substrates

Hiroaki Tatsumi [a,*] , Shunya Nitta [a,b] , Atsushi M. Ito [c,d] , Arimichi Takayama [c,d] ,
Makoto Takahashi [a] , Seongjae Moon [e] , Eiki Tsushima [e] , Hiroshi Nishikawa [a]

[a] Joining and Welding Research Institute, The University of Osaka, 11-1 Mihogaoka, Ibaraki, Osaka 567-0047, Japan
[b] Graduate School of Engineering, The University of Osaka, 2-1 Yamadaoka, Suita, Osaka 565-0871, Japan
[c] National Institute for Fusion Science, National Institutes of Natural Sciences, 322-6 Oroshi-cho, Toki, Gifu 509-5292, Japan
[d] Graduate Institute for Advanced Studies, SOKENDAI, 322-6 Oroshi-cho, Toki, Gifu 509-5292, Japan
[e] FJ Composite Materials Co., LTD., 2-2-3 Kashiwadai Minami, Chitose, Hokkaido 066-0009, Japan

ARTICLE INFO

ABSTRACT

This study elucidates the atomistic mechanisms governing the robust bonding between β-Si$_3$N$_4$ and Cu via a Ti-induced TiN interlayer employing an integrated experimental and computational approach. Density functional theory (DFT) calculations of the potential energy surfaces (PESs) of β-Si$_3$N$_4$ revealed a stronger chemical affinity of Ti compared with other metals. Following Ti deposition, the formation of TiN on β-Si$_3$N$_4$ was confirmed, and transmission electron microscopy (TEM) identified five distinct crystallographic orientation relationships (ORs) at the β-Si$_3$N$_4$/TiN interface. Lattice misfit analysis showed that all ORs exhibited minor mismatches, indicating a structurally adaptable interface. DFT-based adhesion energy calculations for representative ORs confirmed that these low-misfit configurations correspond to energetically stable interfaces exhibiting substantial work of adhesion. Electronic structure analyses revealed strong Ti–N bonds with both covalent and ionic character. These findings suggest that the system's robustness stems from its inherent ability to form multiple, structurally coherent, and strongly bonded interfaces. Notably, thermal cycling tests confirmed the excellent interfacial reliability of the TiN-mediated Cu/β-Si$_3$N$_4$/Cu substrates, with a negligible delamination increase of less than 1% after 4500 cycles between –55 and 150 °C. This study provides direct atomistic insights into the Ti-mediated bonding mechanism and demonstrates the potential of the Cu–β-Si$_3$N$_4$ interface for high-reliability power electronics. Our integrated experimental–computational approach offers a framework for designing advanced metal–ceramic interfaces with optimized crystallographic alignment and adhesion properties.

1. Introduction

The integration of ceramics with metals remains a long-standing challenge in materials science [1], particularly for applications requiring high thermal stability, electrical insulation, and mechanical reliability, such as high-power electronic devices [2–5]. Among ceramics, silicon nitride (β-Si$_3$N$_4$) exhibits excellent thermal conductivity, chemical stability, and structural toughness, making it a promising candidate for next-generation insulating substrates [6,7]. However, the intrinsic chemical stability of β-Si$_3$N$_4$ presents a significant challenge to bonding with metals such as Cu, which are widely used in power modules.

Conventional bonding techniques, such as active metal brazing

(AMB) with Ag-Cu-Ti alloys [8], have partially addressed this limitation by exploiting the chemical reactivity of Ti with β-Si$_3$N$_4$. Nonetheless, these approaches continue to encounter challenges such as void formation owing to filler metal flow [9,10] and reliability degradation caused by thermomechanical stress [11] or Ag migration under electrochemical stress [12]. To address these issues, a growing demand exists for quasi-direct bonding techniques that mitigate liquid–solid interface reactions while ensuring high interfacial reliability. In response, alternative processes—such as direct bonding via localized surface decomposition [13,14] or the deposition of multilayers such as Ti/Cu [15,16] and Ti/TiN/Ti/TiN/Ti [17]—have been proposed. Our previous study also introduced a quasi-direct bonding technique employing thin active metal Ti/Al bilayer deposition, achieving Ag-free,

* Corresponding author.
  E-mail address: tatsumi.jwri@osaka-u.ac.jp (H. Tatsumi).

void-free interfaces [18]. Although these approaches demonstrate clear practical benefits, a more comprehensive understanding of the atomistic interface structures that enable Ti-mediated bonding with β-Si$_3$N$_4$ is essential. In particular, fundamental questions persist regarding the crystallographic configurations that govern the stability of these interfaces.

In the literature, both experimental and computational studies have demonstrated that Ti readily reacts with β-Si$_3$N$_4$ to form TiN at the β-Si$_3$N$_4$–Ti interface [19]. Accordingly, discussions on interfacial stability in β-Si$_3$N$_4$–Ti systems typically focus on the preferred crystallographic orientation relationships (ORs) between β-Si$_3$N$_4$ and TiN. A pioneering study by Iwamoto and Tanaka [20] identified a preferred OR—$[0001]_{\beta-\text{Si}_3\text{N}_4} \| [110]_{\text{TiN}}$ with $(10\bar{1}0)_{\beta-\text{Si}_3\text{N}_4} \| (111)_{\text{TiN}}$—at the AMB interface employing high-resolution transmission electron microscopy (HRTEM). From a computational perspective, Yang et al. [21] suggested strong bonding at the β-Si$_3$N$_4$/α-Ti interface based on work of separation (or work of adhesion) evaluated by first-principles calculations. More recently, Zhang et al. [22,23] integrated computational and experimental approaches to guide the selection of preferred interface materials, such as AMB filler metals [22] or metallized layers [23], for bonding to β-Si$_3$N$_4$. Despite these advances, knowledge remains limited regarding the diversity of preferred ORs, their lattice mismatch, and their energetic stability at the β-Si$_3$N$_4$/TiN interface. Therefore, a more comprehensive understanding of the atomistic configurations governing interfacial bonding is needed to enable the rational design of high-reliability metal–ceramic joints.

To address these knowledge gaps, this study aims to clarify the atomistic mechanisms of Ti-mediated Cu–β-Si$_3$N$_4$ bonding, employing a combination of experimental analyses and first-principles calculations. First, the potential energy surfaces (PESs) of β-Si$_3$N$_4$, which describe the chemical reactivity of the material surface [24], were calculated to assess the chemical affinity of Ti relative to other metals. After confirming TiN formation on β-Si$_3$N$_4$ via Ti deposition, multiple ORs at the β-Si$_3$N$_4$/TiN interface were experimentally identified via transmission electron microscopy (TEM) and their lattice mismatches were systematically evaluated. Furthermore, first-principles calculations were performed to quantify the work of adhesion (W_{ad}) [23] for representative ORs to clarify their interfacial stability. The charge density difference and the density of states (DOS) were investigated to elucidate the electronic structure at the bonding interface. Finally, the high thermal cycling reliability of the TiN-intermediated Cu/β-Si$_3$N$_4$/Cu substrates was demonstrated through thermal cycling tests (TCTs). This combined experimental and computational approach provides a comprehensive understanding of the atomistic interfacial structures and the reliability of robust Ti-mediated Cu–β-Si$_3$N$_4$ bonding interfaces.

2. Experimental and computational methods

2.1. Experimental procedures

A schematic of the bonding procedure is shown in Fig. 1. Ti was deposited on both sides of a β-Si$_3$N$_4$ substrate (thickness: 0.32 mm) via Ar plasma sputtering with a direct current (DC) power source to a thickness of approximately 200 nm (Fig. 1a). Subsequently, the Ti-deposited β-Si$_3$N$_4$ substrate was stacked between two Cu sheets (thickness: 0.30 mm) and bonded under a vacuum atmosphere of 1×10^{-3} Pa while applying a uniaxial compressive stress of 15 MPa and heating to 950 °C (Fig. 1b). After bonding, Cu patterns were fabricated via chemical etching and diamond-wire saw cutting, as shown in Fig. 1c. Detailed information can be found in our previous study [18].

The surface morphology of the as-deposited β-Si$_3$N$_4$ substrate prior to bonding was characterized employing scanning electron microscopy (SEM, SU-70, Hitachi High-Tech Corporation, Japan) and energy-dispersive X-ray spectroscopy (EDX). The crystal structure of the deposited layer was characterized via grazing incidence X-ray diffraction (GIXRD, SmartLab, Rigaku, Japan) at a low incident angle of 0.5° with a Cu Kα X-ray source (λ = 1.5406 Å, 45 kV, 200 mA). The cross-sectional microstructure at the bonding interface between β-Si$_3$N$_4$ and Cu was analyzed via SEM using an Ar-ion beam cross-sectional polisher (SM-09,010, JEOL Ltd., Japan). The interfacial crystalline structure was further evaluated via TEM (JEM-2100F, JEOL Ltd., Japan). TEM samples were prepared utilizing a focused ion beam (FIB, FB-2000A, Hitachi Ltd., Japan).

To investigate thermal cycling reliability, the Ti-mediated Cu/β-Si$_3$N$_4$/Cu substrates were subjected to TCT up to 4500 cycles between −55 and 150 °C using a thermal cycling chamber (TSE-12, ESPEC Corp., Japan). The test conditions followed the JEDEC standard (JESD22-A104). This temperature range was selected owing to its common application in power electronics reliability testing, and the number of cycles was extended to demonstrate superior long-term performance. Nondestructive inspections were performed every 300 cycles employing scanning acoustic tomography (SAT, FS100III, Hitachi Ltd., Japan).
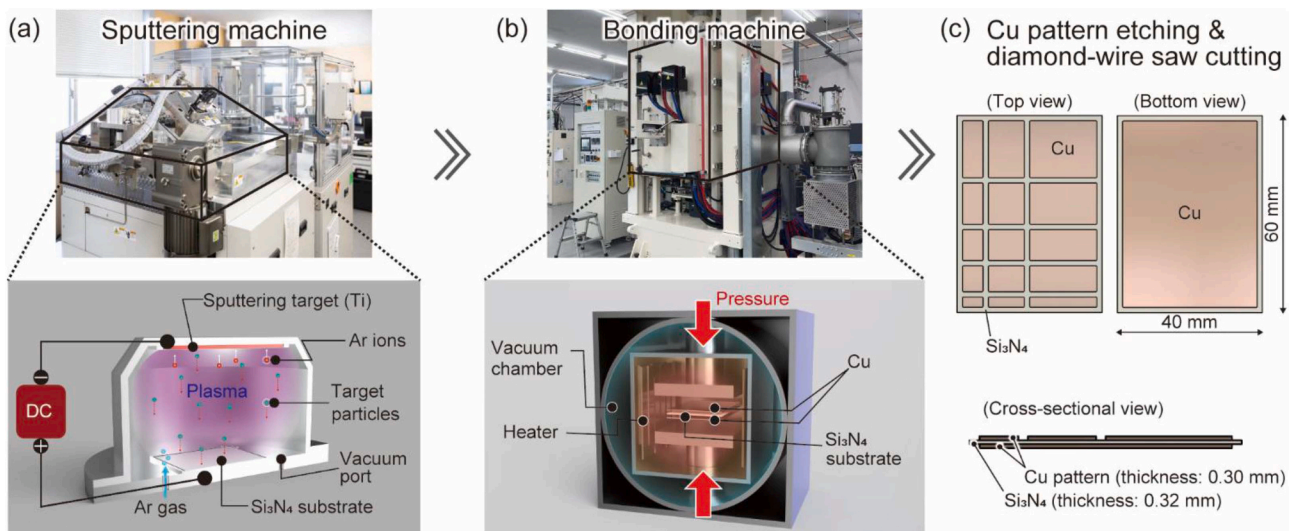
Fig. 1. Schematic of the fabrication process for the Ti-mediated Cu/β-Si$_3$N$_4$/Cu substrate: (a) Ti deposition onto both sides of the β-Si$_3$N$_4$ substrate; (b) bonding with Cu sheets under uniaxial pressure; (c) Cu patterning and sample cutting.

2.2. Computational methods

First-principles calculations of the potential energies between β-Si_3N_4 and the deposited layers were performed using the "OpenMX" code package [25,26] based on DFT, as shown in Fig. 2. The generalized gradient approximation (GGA) with the Perdew-Burke-Ernzerhof (PBE) functional [27] was used for the exchange-correlation potential. Core electrons were treated as frozen, and valence electrons were described using norm-conserving pseudo-potentials generated via the Morrison-Bylander-Kleinman method [28]. Valence electron orbitals were represented as a linear combination of atomic orbitals (LCAO), where the orbitals are numerically generated [25,26]. The accuracy of the OpenMX code and pseudo-potentials was confirmed in delta factor [29]. Detailed computational parameters, including the specifications of the basis sets and convergence criteria for structural relaxation, are provided in Appendix A.

First, the PESs of the β-Si_3N_4 surface, representing energy changes owing to adatom adsorption on the surface, were analyzed to investigate the affinity between the deposition materials and the β-Si_3N_4 surface. A β-Si_3N_4(0001) surface slab model (Fig. 2a) was constructed for the PES calculations. Because the β-Si_3N_4(0001) surface is polar, the effective screening medium (ESM) method [30,31] was applied to eliminate the artificial electric field caused by periodic boundary conditions. The surface was created by introducing a 30-Å vacuum layer into the bulk β-Si_3N_4 model with a $1 \times 1 \times 3$ supercell while satisfying the periodic boundary conditions. Based on feasibility tests conducted beforehand, a model with three β-Si_3N_4 layers (thickness: 8.59 Å) was adopted, given the balance between computational efficiency and accuracy. A cutoff energy of 160 Hartree (4354 eV) was set for the plane wave basis, and a k-point grid of $4 \times 4 \times 1$ was used for all calculations. Structural relaxation was performed for all atoms to obtain the optimized β-Si_3N_4(0001) surface configuration, and the total energy of the β-Si_3N_4(0001) surface model before adsorption, $E_{slab,\beta-Si_3N_4}$, was determined. In addition, the total energy of a single atom, E_{adatom}, was calculated. An adatom was then placed at one of the positions in the evenly spaced 6×6 in-plane grid on the β-Si_3N_4(0001) surface at an initial distance of 2 Å from the surface. The total energy of the

β-Si_3N_4(0001) surface slab model with an adatom adsorbed at (x, y), $E_{adsorbed}(x, y)$, was obtained after relaxation. For each (x, y) grid point, the adatom was fully relaxed along the z-direction to find its minimum-energy height, while its (x, y) position was kept fixed. Thus, the PESs, $E_{PES}(x,y)$, was defined as the total energy difference before and after adatom adsorption, as follows:

$$E_{PES}(x, y) = E_{adsorbed}(x, y) - \left(E_{slab,\beta-Si_3N_4} + E_{adatom}\right). \tag{1}$$

To evaluate the atomistic stability of the bonding interface, DFT calculations were conducted following the scheme in Fig. 2b In the first step (Fig. 2b-1), bulk structures of Materials A and B were fully relaxed, enabling simultaneous optimization of both supercell dimensions and atomic positions to determine their equilibrium lattice parameters and total energies (E_{bulk}). In the second step (Fig. 2b-2), surface slab models were constructed by cleaving the relaxed bulk structures along selected crystallographic planes and introducing a 30-Å vacuum layer along the z direction. During this step, both the atomic positions and supercell dimensions were relaxed to obtain the total energies of the surface slab models (E_{slab}). Finally, interface slab models were constructed by joining the relaxed surface slab models of Materials A and B (Fig. 2b-3). In these models, both the atomic positions and supercell dimensions were relaxed to calculate the total energies of the interface systems ($E_{interface}$). Unit cell repetitions along in-plane directions were adjusted to satisfy periodic boundary conditions with minimal lattice misfit. The k-point grid was set to 4–8 divisions for each x, y, and z direction in the bulk models (Step 1), depending on the supercell size, and 4–8 divisions for x and y, with a single division for z, in the slab models (Steps 2 and 3).

3. Results and discussion

3.1. Deposition material selection

To achieve a strong bonding interface, selecting a deposition material with high affinity for β-Si_3N_4 is crucial. Therefore, we conducted a broad survey of the PESs of β-Si_3N_4 for the adsorption of four candidate metals (Ti, Al, Ag, and Cu) to clarify differences in their chemical affinities. Ti and Al exhibit high reactivity with ceramics, Ag is a noble
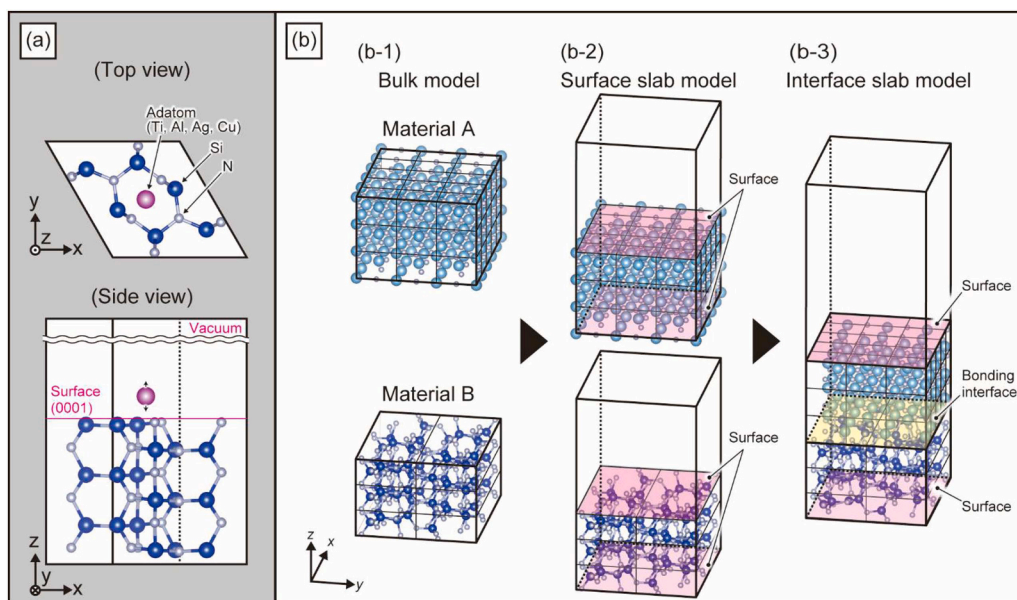
Fig. 2. DFT models for (a) PES calculation—adsorption of Ti, Al, Ag, or Cu adatoms on a β-Si_3N_4(0001) surface—and (b) W_{ad} calculation of the bonding interface: (b-1) Bulk models of Materials A and B were fully relaxed to obtain equilibrium structures and bulk energies (E_{bulk}). (b-2) Surface slab models with a 30-Å vacuum layer were constructed; atomic positions and supercell dimensions were relaxed to calculate slab energies (E_{slab}). (b-3) An interface slab model was developed by joining the two slabs; atomic positions and supercell dimensions were relaxed to obtain interface energy ($E_{interface}$). The x and y supercell dimensions were initially averaged to maintain periodic boundary conditions before relaxation.
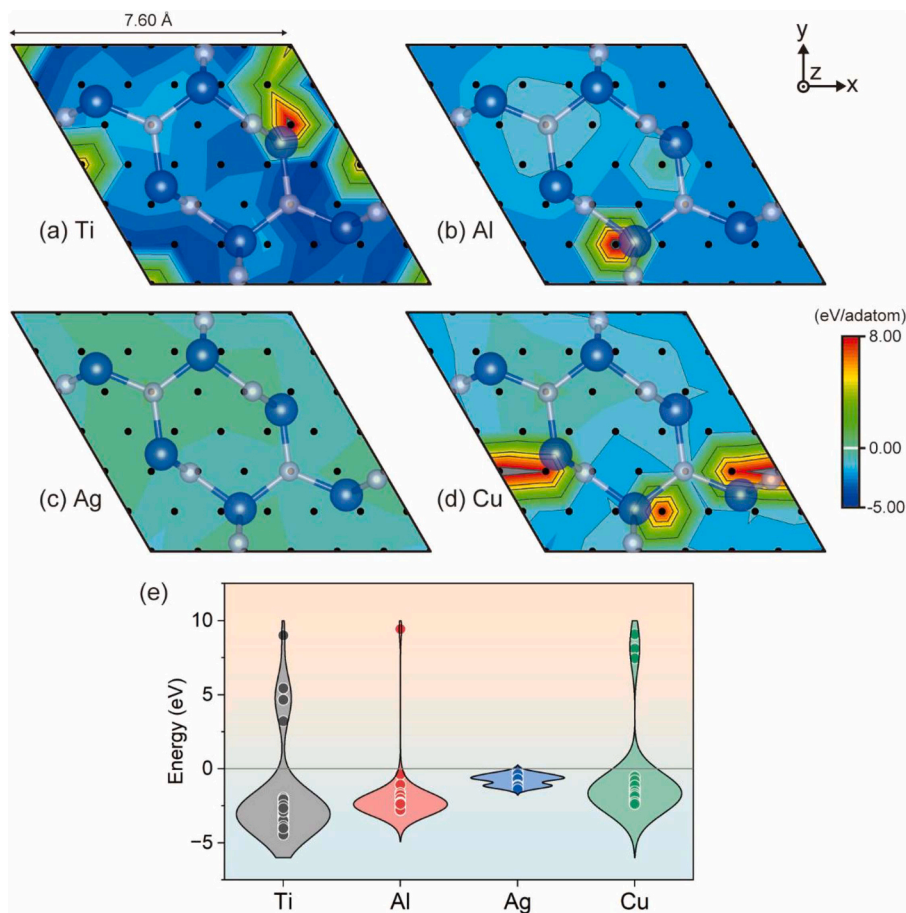
Fig. 3. PESs of the β-Si$_3$N$_4$(0001) surface for adatom adsorption (Ti, Al, Ag, or Cu): (a–d) PES maps for Ti, Al, Ag, and Cu adatoms on the β-Si$_3$N$_4$ surface, respectively, where color indicates the adsorption energy (eV/adatom). Lower energy values represent more stable adsorption sites. The black dots indicate the actual positions where adsorption energy calculations were performed. (e) Violin plot summarizing the distribution of calculated adsorption energies for each metal, with individual data points overlaid.

metal with low reactivity, and Cu is the bonded material used in this study. The calculated PESs are presented in Fig. 3. Fig. 3a–d present the PESs of the β-Si$_3$N$_4$(0001) surface for the adsorption of Ti, Al, Ag, and Cu, respectively. As shown in Fig. 3a, Ti exhibits a wide distribution of highly stable adsorption sites of approximately −4 eV/adatom. By contrast, Al, Ag, and Cu show relatively higher PES values, ranging from −2 to −1 eV/adatom, as shown in Figs. 3(b–d). Furthermore, the $E_{PES}(x, y)$ values for all calculated points (Fig. 3e) indicate that Ti has more stable adsorption sites with the lower energy states compared with the other three metals.

To quantitatively compare overall surface affinities, the canonical average energy was calculated. This provides a more physically representative metric than a simple average by weighting the higher occupation probability of more stable sites. The average energy, $\overline{E}$, is expressed as follows:

$$\overline{E} = \sum_n E_n P_n = \frac{\sum_n E_n e^{-E_n/k_B T}}{\sum_n e^{-E_n/k_B T}}, \tag{2}$$

where E_n represents the adsorption energy at site n, k_B is the Boltzmann constant, P_n is the probability distribution (canonical distribution), and T is the absolute temperature. At the bonding temperature (950 °C, 1223 K), the calculated average energies were approximately −4.38 eV for Ti, −2.74 eV for Al, −2.28 eV for Cu, and −1.25 eV for Ag. This result confirms that Ti exhibits the highest chemical affinity for the β-Si$_3$N$_4$ surface.

This finding was further supported by peeling tests conducted on

bonded specimens, provided in Appendix B. In these tests, Ti, Al, and Ag were deposited onto the β-Si$_3$N$_4$ surface prior to bonding, or bonding was performed without any deposition. The results (Fig. A1) show that Ti-coated specimens exhibited the highest bonding strength, consistent with their strong adsorption affinity predicted by the PES calculations.

3.2. Characterization of Ti deposition layer

To evaluate the characteristics of the Ti deposition layer formed on the β-Si$_3$N$_4$ surface, microstructural, elemental, and crystallographic analyses were conducted, as shown in Fig. 4. The SEM image of the Ti deposition layer (Fig. 4a) shows a typical uneven surface morphology [32], which is attributed to the irregular shape of the raw β-Si$_3$N$_4$ powders. Elemental mappings of Si, N, and Ti using EDX (Fig. 4b) indicate that Ti was uniformly distributed across the β-Si$_3$N$_4$ surface. The GIXRD diffraction pattern (Fig. 4c) shows diffraction peaks corresponding to β-Si$_3$N$_4$ (P6$_3$/m, $a = b = 7.602$ Å, $c = 2.907$ Å) and TiN (Fm$\overline{3}$m, $a = b = c = 4.241$ Å); however, no detectable peaks corresponding to Ti were observed. Although Ti may remain in an amorphous form or in quantities below the detection limit, the results suggest that most of the deposited Ti reacts with β-Si$_3$N$_4$ to form a TiN layer. The reaction, Si$_3$N$_4$(s) + 4Ti(s) = 4TiN(s) + 3Si(s), is thermodynamically favorable with a negative Gibbs free energy of reaction [18,19]. Despite the absence of Si byproduct in the GIXRD analysis, likely owing to its poor crystallinity after deposition, the identification of distinct TiN peaks validated that this reaction occurred during sputtering. These results verify that the Ti deposition layer chemically reacted with the
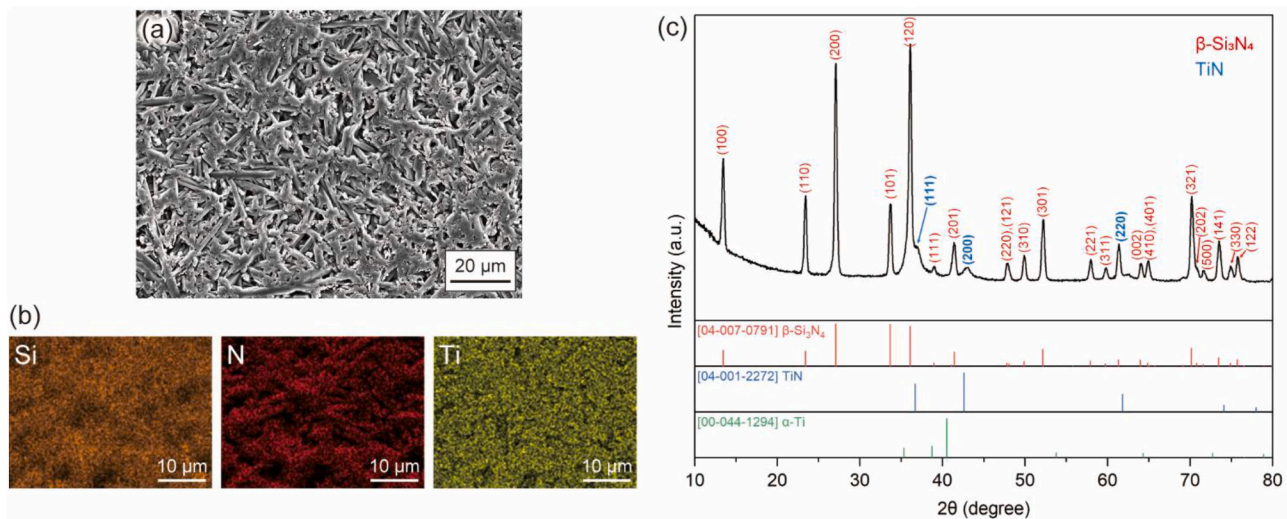
Fig. 4. Characterization of the Ti deposition layer on the β-Si₃N₄ surface: (a) SEM image of the as-deposited surface. (b) Elemental mapping of Si, N, and Ti using EDX on the β-Si₃N₄ surface. (c) GIXRD diffraction pattern showing the presence of β-Si₃N₄ and TiN with no detectable Ti peaks.

β-Si₃N₄ surface, forming a TiN layer that likely enhances interfacial bonding.

3.3. Interfacial structure of β-Si₃N₄/Cu joint with the Ti-mediated layer

To clarify the interfacial structure between β-Si₃N₄ and Cu with a Ti-mediated layer, cross-sectional observations and elemental analyses were performed, as shown in Fig. 5. Fig. 5a presents a low-magnification SEM image of the Ti-mediated β-Si₃N₄/Cu joint interface, revealing the formation of an intermediate layer. The magnified TEM bright field (BF) image in Fig. 5b shows a distinct intermediate layer at the bonding interface, with a thickness of several hundred nanometers. Fig. 5c–h
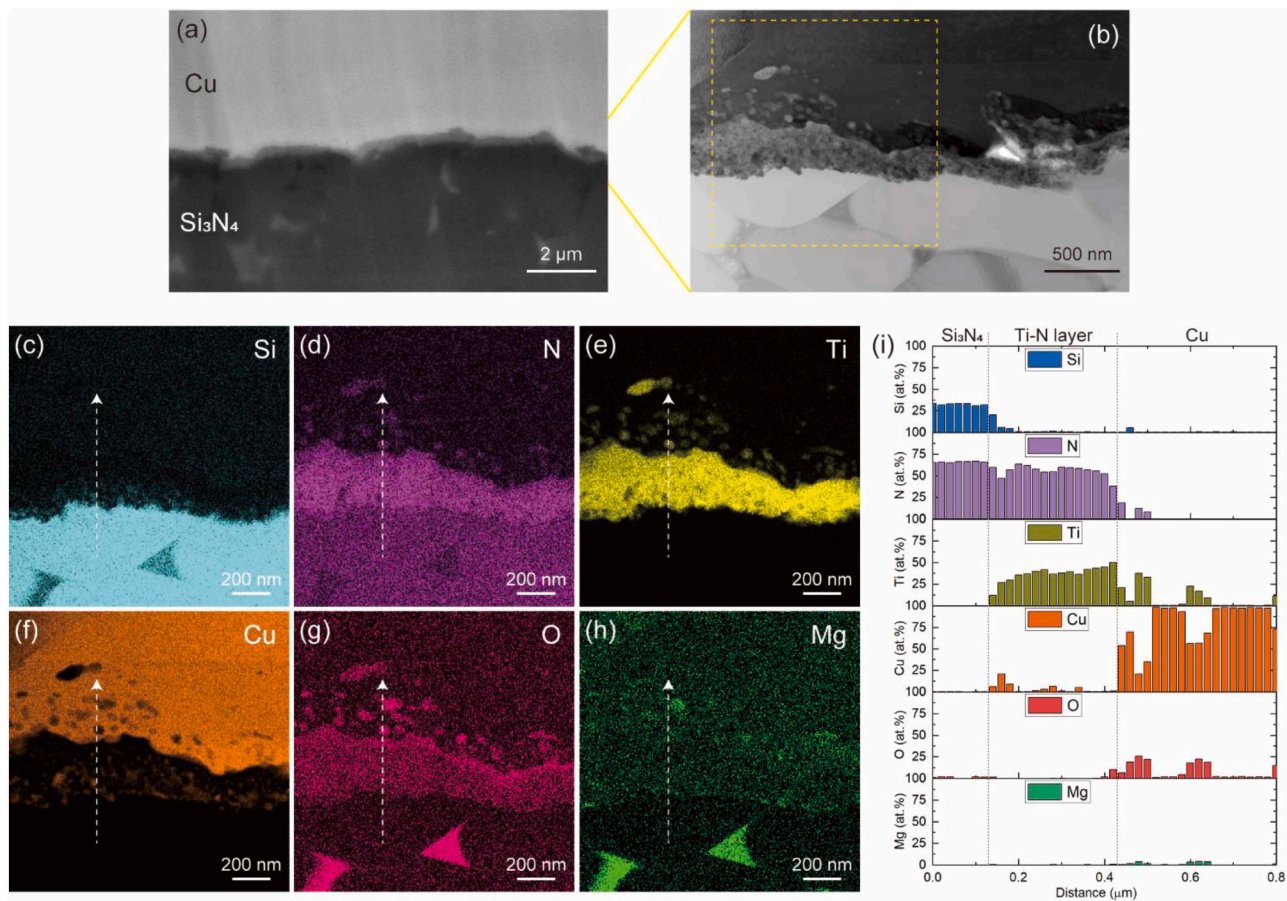

Fig. 5. Cross-sectional observation results of the Ti-mediated β-Si₃N₄/Cu interface: (a) SEM image of the interface; (b) TEM BF image showing a magnified view of the dashed region in (a); (c–h) EDX elemental mappings of Si, N, Ti, Cu, O, and Mg in the region shown in (b); (i) line analysis along the dashed white lines in (c–h), confirming the formation of a TiN intermediate layer.

show the elemental mapping results of the dashed-line region in Fig. 5b, confirming the formation of a TiN intermediate layer between β-Si₃N₄ and Cu. Line analysis along the dashed line in Fig. 5i further supports the identification of this intermediate layer as TiN. Notably, a trace amount of Ti was also detected within the Cu layer, indicating that some unreacted Ti diffused into the Cu during the 950 °C bonding process. From a thermodynamic perspective, the Cu–Ti binary phase diagram indicates that Cu exhibits finite solid solubility for Ti at this temperature [33]. This provides a driving force for the residual Ti to diffuse into the Cu matrix, thereby establishing metallurgical continuity at the TiN/Cu interface. Consequently, such results confirmed that β-Si₃N₄ and Cu were bonded via a TiN intermediate layer, indicating that the atomic structure of the β-Si₃N₄/TiN interface plays a critical role in determining the reliability of the Ti-mediated β-Si₃N₄/Cu joint.

To further investigate the interfacial crystalline structure between β-Si₃N₄ and TiN, selected area electron diffraction (SAED) analyses were performed near the interface, as shown in Fig. 6. The interfacial structures were determined by analyzing superimposed SAED patterns obtained by maintaining a fixed sample orientation while shifting the electron beam between the β-Si₃N₄ substrate and adjacent TiN grains. Fig. 6a presents a BF TEM image wherein points A, B, C, and D are marked as the locations where SAED patterns were acquired. These measurements enabled a crystallographic analysis of both the single-crystalline β-Si₃N₄ and adjacent polycrystalline TiN phases at several positions near the interface. At Point A (Fig. 6b), an SAED pattern corresponding to β-Si₃N₄ with the $[10\bar{1}0]$ zone axis was obtained. At points B and C (Fig. 6c,d), SAED patterns corresponding to TiN with the [110] zone axis were obtained. At point B, TiN(002) was aligned parallel to
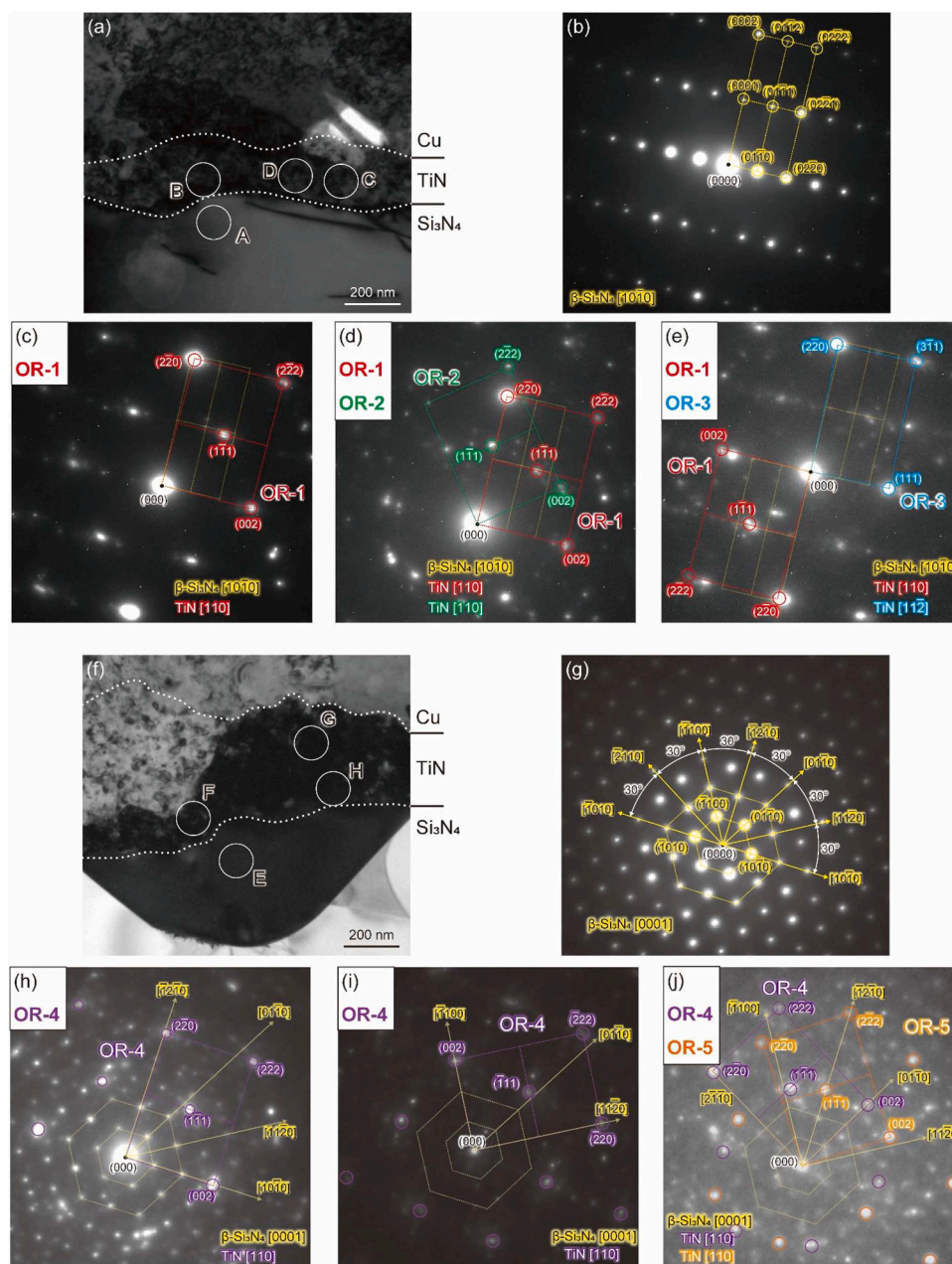
Fig. 6. SAED analysis of the β-Si₃N₄/TiN interface identifying ORs: (a) BF TEM image showing points A–D; (b) SAED pattern at point A, indexed to β-Si₃N₄; (c–e) SAED patterns at points B, C, and D, respectively, indexed to TiN; (f) BF TEM image showing points E–H; (g) SAED pattern at point E, indexed to β-Si₃N₄; (h–j) SAED patterns at points F, G, and H, respectively, indexed to TiN. These diffraction patterns correspond to five distinct ORs (OR-1 to OR-5) observed at the β-Si₃N₄/TiN interface. In (c–e, h–j), the semi-transparent yellow pattern serves as a visual reference for the adjacent β-Si₃N₄ crystal (determined from (b) or (g)).

β-Si$_3$N$_4$(01$\bar{1}$0), defined as orientation relationship 1 (OR-1), whereas at point C, TiN(1$\bar{1}$1) was aligned parallel to β-Si$_3$N$_4$(0001) (OR-2). At point D (Fig. 6e), an SAED pattern corresponding to TiN with the [11$\bar{2}$] zone axis was obtained, where TiN(2$\bar{2}$0) was aligned parallel to β-Si$_3$N$_4$(0001) (OR-3). An additional BF TEM image is shown in Fig. 6f, wherein points E, F, G, and H are marked as the locations where SAED patterns were acquired. At point E (Fig. 6g), an SAED pattern corresponding to β-Si$_3$N$_4$ with the [0001] zone axis was obtained. At points F, G, and H (Fig. 6h–j), SAED patterns corresponding to TiN with the [110] zone axis were obtained, where TiN(002) was aligned parallel to β-Si$_3$N$_4$(10$\bar{1}$0) (OR-4). In addition, at point H, an SAED pattern was observed with TiN(2$\bar{2}$0) aligned parallel to β-Si$_3$N$_4$(0001) (OR-5). These observations validate the presence of five distinct ORs (OR-1 through OR-5) at the β-Si$_3$N$_4$/TiN interface. The diversity of these ORs suggests that multiple energetically favorable configurations can coexist at the interface, which may enhance the structural integrity and bonding reliability of the TiN-intermediated β-Si$_3$N$_4$–Cu joint.

### 3.4. Atomistic evaluation of the β-Si$_3$N$_4$/TiN interface

Idealized SAED patterns were simulated, as shown in Fig. 7, to quantitatively evaluate the lattice misfit of the experimentally observed ORs. This approach facilitates precise analysis, free from experimental artifacts. Fig. 7a–c show schematic models of atomic configurations of β-Si$_3$N$_4$ and TiN, including representative lattice planes. Fig. 7d–h illustrate the simulated SAED patterns for OR-1 through OR-5, with

lattice planes of β-Si$_3$N$_4$ (black dots) and TiN (red dots). The regions highlighted by circles indicate close proximity between the lattice planes of the two crystals, suggesting lattice matching in each OR case. The patterns clearly demonstrate the well-aligned lattice planes between β-Si$_3$N$_4$ and TiN across all five ORs. To quantitatively assess the interface lattice misfit, the Bramfitt two-dimensional misfit method was used, defined as follows [34]:

$$\delta^{(hkl)_{TiN}}_{(hkl)_{\beta-Si_3N_4}} = \frac{1}{3}\sum_{i=1}^{3} \frac{\left| d^i_{[uvw]_{\beta-Si_3N_4}} \cos\theta - d^i_{[uvw]_{TiN}} \right|}{d^i_{[uvw]_{TiN}}} \times 100 \ (\%), \qquad (3)$$

where $(hkl)_{\beta-Si_3N_4}$ and $(hkl)_{TiN}$ are the lattice planes of β-Si$_3$N$_4$ and TiN, respectively, involved in the zone axes; $[uvw]_{\beta-Si_3N_4}$ and $[uvw]_{TiN}$ are the in-plane crystallographic directions of β-Si$_3$N$_4$ and TiN, respectively, on the (hkl) plane; d is the interatomic spacing along $[uvw]_{TiN}$; θ is the angle between the $[uvw]_{\beta-Si_3N_4}$ and $[uvw]_{TiN}$. This method involves selecting three sets of major lattice vectors with the closest interatomic spacing and angles from the superimposed diffraction patterns of the two crystals observed along a common zone axis. The calculated in-plane lattice misfits for the five ORs are listed in Table 1 as 2.49, 2.72, 6.24, 4.77, and 2.69 % for OR-1 through OR-5, respectively. These results indicate excellent lattice matching in all cases, highlighting the inherent structural flexibility of the β-Si$_3$N$_4$/TiN interface facilitating robust bonding.

The experimental identification of five distinct ORs with low lattice misfits validated the inherent structural flexibility of the β-Si$_3$N$_4$/TiN interface. However, interfacial stability also critically depends on the
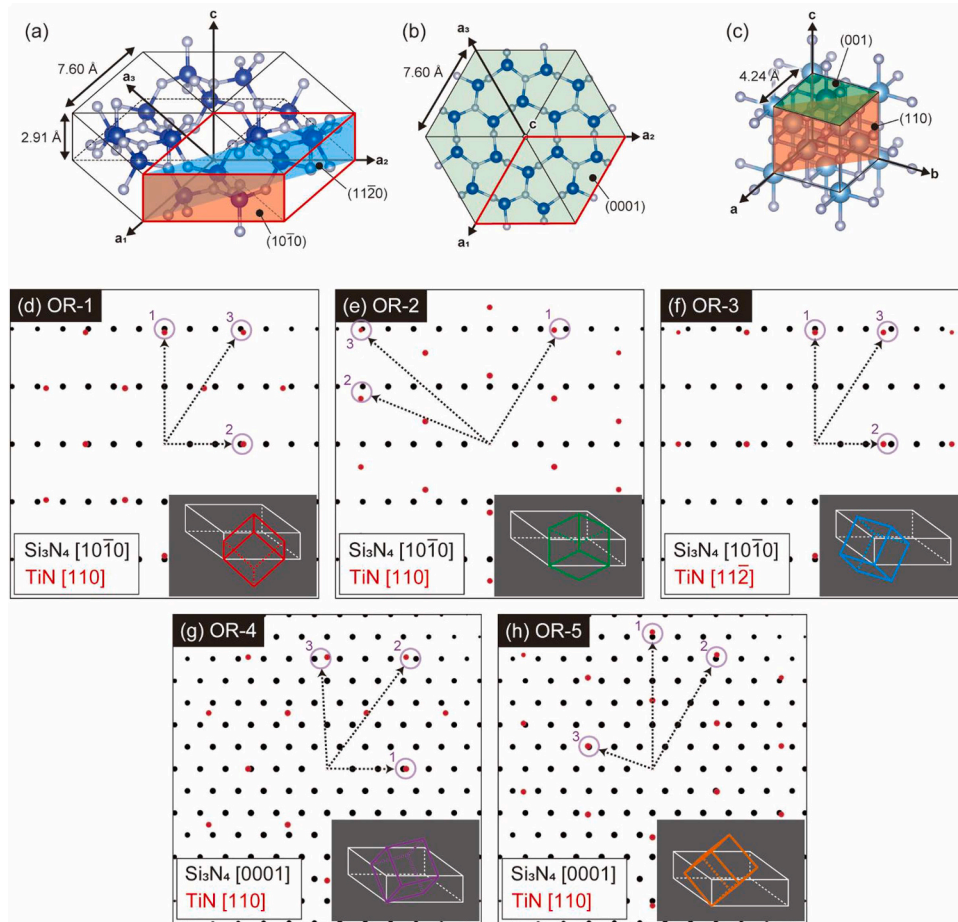
Fig. 7. Crystal structures of β-Si$_3$N$_4$ and TiN, and simulated SAED patterns for the five ORs experimentally identified in Fig. 6: (a) crystal structure of β-Si$_3$N$_4$ and (b) its in-plane view along the [0001] direction. (c) Crystal structure of TiN. (d–h) Simulated SAED patterns of TiN (red dots) on β-Si$_3$N$_4$ (black dots) corresponding to OR-1 through OR-5, respectively. Insets show the 3D orientation alignments of β-Si$_3$N$_4$ (white) and TiN (colored), highlighting the specific crystallographic relationship in each case.

Table 1
Planar lattice misfit in the ORs between β-Si₃N₄ and TiN obtained in this study.

ORs	i	$[uvw]_{\beta-\mathrm{Si_3N_4}}$	$d_{[uvw]\beta-\mathrm{Si_3N_4}}$ (Å)	$[uvw]_{\mathrm{TiN}}$	$d_{[uvw]\mathrm{TiN}}$ (Å)	θ (degree)	δ (%)
OR-1	1	[0002]	1.454	[2̄20]	1.499	0.000	2.49 %
$[10\bar{1}0]_{\beta-\mathrm{Si_3N_4}}\|[110]_{\mathrm{TiN}}$	2	[03̄30]	2.194	[002]	2.121	0.000	
$(01\bar{1}0)_{\beta-\mathrm{Si_3N_4}}\|(002)_{\mathrm{TiN}}$	3	[03̄32]	1.212	[2̄22]	1.224	−1.744	
OR-2	1	[03̄32]	1.212	[11̄3]	1.279	4.024	2.72 %
$[10\bar{1}0]_{\beta-\mathrm{Si_3N_4}}\|[110]_{\mathrm{TiN}}$	2	[05̄51]	1.199	[2̄22̄]	1.224	4.896	
$(0001)_{\beta-\mathrm{Si_3N_4}}\|(1\bar{1}1)_{\mathrm{TiN}}$	3	[05̄52]	0.976	[33̄1̄]	0.973	0.301	
OR-3	1	[0002]	1.454	[2̄20]	1.499	0.000	6.24 %
$[10\bar{1}0]_{\beta-\mathrm{Si_3N_4}}\|[11\bar{2}]_{\mathrm{TiN}}$	2	[03̄30]	2.194	[111]	2.449	0.000	
$(0001)_{\beta-\mathrm{Si_3N_4}}\|(2\bar{2}0)_{\mathrm{TiN}}$	3	[03̄32]	1.212	[31̄1]	1.279	2.038	
OR-4	1	[303̄0]	2.194	[002]	2.121	0.000	4.77 %
$[0001]_{\beta-\mathrm{Si_3N_4}}\|[110]_{\mathrm{TiN}}$	2	[03̄30]	2.194	[11̄1]	2.449	−5.264	
$(10\bar{1}0)_{\beta-\mathrm{Si_3N_4}}\|(002)_{\mathrm{TiN}}$	3	[3̄52̄0]	1.510	[2̄20]	1.499	−6.587	
OR-5	1	[3̄63̄0]	1.267	[2̄22]	1.224	0.000	2.69 %
$[0001]_{\beta-\mathrm{Si_3N_4}}\|[110]_{\mathrm{TiN}}$	2	[05̄50]	1.317	[11̄3]	1.279	0.504	
$(\bar{1}2\bar{1}0)_{\beta-\mathrm{Si_3N_4}}\|(1\bar{1}1)_{\mathrm{TiN}}$	3	[3̄120]	2.488	[11̄1̄]	2.449	−0.364	

chemical bonding state. To elucidate this, DFT calculations were performed to estimate W_{ad}, charge density difference, and DOS for representative cases selected from the experimentally observed ORs, as shown in Fig. 8. Two ORs were selected: OR-1, which exhibits the lowest lattice misfit, and OR-2, which involves close-packed surfaces of both materials. As regards OR-1, because SAED analysis does not uniquely determine the interface plane, three low-indexed interface planes—$[0001]_{\beta-\mathrm{Si_3N_4}}\|[01\bar{1}]_{\mathrm{TiN}}$, $[01\bar{1}0]_{\beta-\mathrm{Si_3N_4}}\|[100]_{\mathrm{TiN}}$, and $[2\bar{1}\bar{1}0]_{\beta-\mathrm{Si_3N_4}}\|[011]_{\mathrm{TiN}}$—were modeled as OR-1(a), OR-1(b), and OR-1 (c), respectively (Fig. 8a–c). For OR-2, since the TiN(111) plane can be terminated by either Ti or N atoms, both Ti- and N-terminated interface models were modeled as OR-2(Ti) and OR-2(N) (Fig. 8d). The number of unit cells along the in-plane x and y directions was carefully adjusted to minimize lattice misfit while ensuring periodic boundary conditions, resulting in-plane strains of less than ±2.3 %. The total number of atoms in each supercell ranged from 116 to 348, depending on the configuration. K-point grids of 4 × 4 × 4, 4 × 8 × 4, 8 × 4 × 4, and 4 × 4 × 4 on bulk models and 4 × 4 × 1, 4 × 8 × 1, 8 × 4 × 1, and 4 × 4 × 1 on slab models were used for OR-1(a), (b), (c), and OR-2, respectively. Prior to these calculations, the reliability of the DFT method was validated by comparing the calculated lattice parameters and surface energies of β-Si₃N₄ and TiN with reported values, as summarized in Appendix C. W_{ad} was calculated using the following equation:

$$W_{ad} = \frac{E_{\mathrm{slab},\,\beta-\mathrm{Si_3N_4}} + E_{\mathrm{slab,\,TiN}} - E_{\mathrm{interface}}}{A}, \tag{4}$$

where $E_{\mathrm{slab},\,\beta-\mathrm{Si_3N_4}}$ and $E_{\mathrm{slab,TiN}}$ are the total energies of the relaxed surface slab models, $E_{\mathrm{interface}}$ is the total energy of the relaxed interface slab model, and A is the interface area.

As shown in Fig. 8e, the calculated W_{ad} values for the interfaces of OR-1(a), OR-1(b), OR-1(c), OR-2(Ti), and OR-2(N) are 1.56, 1.00, 1.58, 3.59, and 1.04 J/m², respectively. These positive and high values indicate that the experimentally observed low-misfit ORs correspond to thermodynamically stable interfaces. Despite these DFT calculations being performed at 0 K, the energetic differences are expected to remain valid at high temperatures, as the vibrational free energy contribution is reportedly an order of magnitude smaller than the calculated energy differences [35]. Although a previous study [20] reported an OR at the β-Si₃N₄/TiN interface formed by the AMB process (corresponding to OR-4 in this study), this study is the first to quantify W_{ad} for experimentally observed ORs using DFT. Our results demonstrate that the β-Si₃N₄/TiN interfaces can form multiple structurally coherent interfaces. Notably, the OR-2(Ti) interface exhibited a remarkably high W_{ad} of 3.59 J/m², as listed in Table 2, despite exhibiting a similar lattice

misfit to the others, strongly suggesting that interfacial stability is governed not only by structural lattice matching but also by the chemical bonding state.

To investigate the impact of the chemical bonding state, the distribution of the charge density difference for OR-1(a)—which includes both Ti–N and Si–N bonds at its interface—was analyzed, as shown in Fig. 8f. On the interfacial Ti–N bond, a significant accumulation of charge (red regions) between the Ti and N atoms indicates the formation of strong covalent bonds. Concurrently, the charge depletion around the Ti atoms (blue regions) reveals a clear charge transfer to the N atoms, indicating an ionic character. Therefore, the Ti–N bond exhibits both covalent and ionic characteristics. Similarly, although less pronounced, charge accumulation between Si and N atoms and a charge transfer from Si to N were observed, suggesting that Si–N bonds also possess both covalent and ionic characteristics. To further elucidate the chemical bonding states, DOS and partial DOS of the Ti–N and Si–N bonds were performed, as shown in Figs. 8g,h. For the Ti–N bond at the interface (Fig. 8g), a significant overlap of DOS between Ti and N, particularly Ti-d and N-p orbitals, was observed across a wide energy range (approximately −8 to −1 eV), indicating strong orbital hybridization and covalent bonding. The Si–N bond (Fig. 8h) also showed an overlap of DOS between Si-p and N-p orbitals, indicating covalent bonding through orbital hybridization.

These electronic structure analyses clarified the origin of the high adhesion energies. Comparison of the charge density difference and DOS results for the Ti–N and Si–N bonds revealed that the interfacial Ti–N bond is the dominant contributor to adhesion. Although Si–N interactions are present, the significant charge transfer and pronounced hybridization between Ti-d and N-p orbitals demonstrate a stronger chemical bond. This finding is consistent with the substantially higher W_{ad} of OR-2(Ti) compared with the others. Therefore, the robust bonding observed in this study is attributed to two complementary mechanisms: (i) structural adaptability that allows multiple low-misfit interfaces and (ii) strong chemical adhesion at these interfaces, primarily driven by Ti–N bonds.

3.5. Thermal cycling reliability of Ti-mediated Cu/β-Si₃N₄/Cu substrates

The thermal cycling reliability of a metal–ceramic joint is primarily determined by the intrinsic strength of its interface against delamination caused by thermal stress [8]. To verify that the favorable atomic structure translates into robust macroscopic performance, the thermal cycling reliability of the TiN-intermediated Cu/β-Si₃N₄/Cu substrate was evaluated via TCT in the temperature range of −55 to 150 °C, as shown in Fig. 9. The geometry and dimensions of the tested insulated circuit
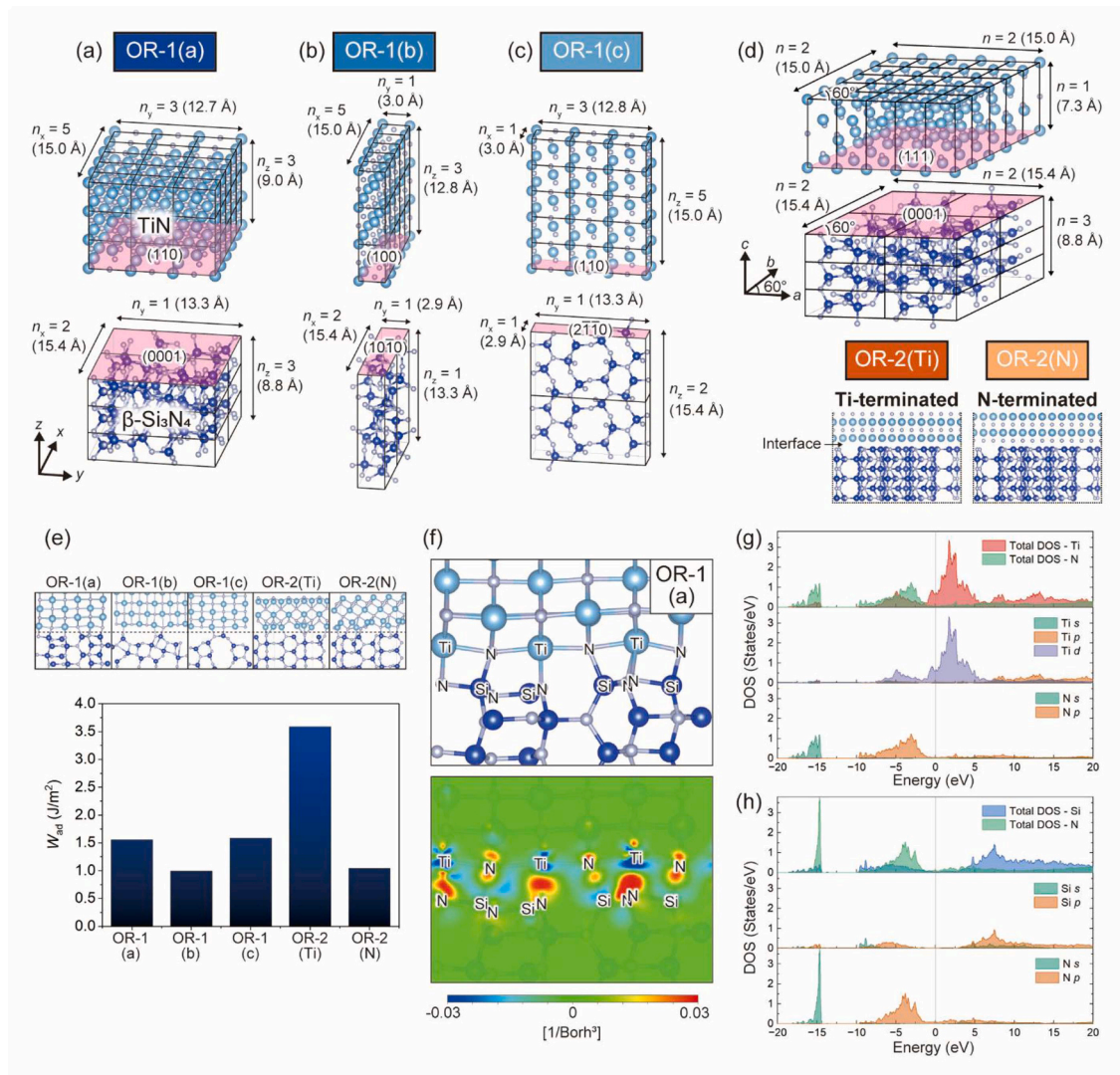
Fig. 8. DFT models and analysis of the β-Si₃N₄/TiN interfaces derived from OR-1 and OR-2. (a–d) Atomic models of the TiN and β-Si₃N₄ slabs for (a) OR-1(a), (b) OR-1(b), and (c) OR-1(c). (d) Atomic model for the OR-2 interface, illustrating both Ti-terminated and N-terminated configurations. (e) Calculated W_{ad} values for the five interface models, with interfacial atom configurations. (f) Cross-sectional plot of the charge density difference for the β-Si₃N₄/TiN interface (OR-1(a)), with red and blue indicating charge accumulation and depletion, respectively. (g) DOS of the Ti–N bond at the β-Si₃N₄/TiN interface; total DOS of Ti and N atoms, PDOS for Ti (s, p, d-orbitals) atom, and PDOS for N (s, p-orbitals) atom. (h) DOS of Si-N bond; total DOS of Si and N atoms, PDOS for Si (s, p-orbitals) atom, and PDOS for N (s, p-orbitals) atom.

Table 2
Details of the DFT interface models constructed for five interface plane candidates (OR-1(a,b,c) and OR-2(Ti,N)) derived from the experimentally identified ORs. For each case, the crystallographic directions along the x, y, and z axes (with z normal to the interface plane) are listed for β-Si₃N₄ and TiN, along with the corresponding in-plane strains in TiN (ε_{TiN}). Also provided are the number of unit cells repeated in each direction (n_x, n_y, n_z), the total number of atoms (N_{at}) in the supercell, and the calculated W_{ad} values.

OR	$x_{\beta-Si_3N_4} \| x_{TiN}$ (ε_{TiN})	$y_{\beta-Si_3N_4} \| y_{TiN}$ (ε_{TiN})	$z_{\beta-Si_3N_4} \| z_{TiN}$	$\beta - Si_3N_4 : n_x, n_y, n_z$ TiN : n_x, n_y, n_z	N_{at}	W_{ad} (J/m²)
OR-1 (a)	[2$\bar{1}\bar{1}$0] ‖ [011] (+ 1.3%)	[01$\bar{1}$0] ‖ [100] (+ 2.3%)	[0001] ‖ [01$\bar{1}$]	$\beta - Si_3N_4$: 2 × 1 × 3 TiN : 5 × 3 × 3	348	1.56
OR-1 (b)	[2$\bar{1}\bar{1}$0] ‖ [011] (+ 1.3%)	[0001] ‖ [01$\bar{1}$] (− 1.0%)	[01$\bar{1}$0] ‖ [100]	$\beta - Si_3N_4$: 2 × 1 × 1 TiN : 5 × 1 × 3	116	1.00
OR-1 (c)	[0001] ‖ [01$\bar{1}$] (− 1.0%)	[01$\bar{1}$0]‖[100] (+ 2.3%)	[2$\bar{1}\bar{1}$0] ‖ [011]	$\beta - Si_3N_4$: 1 × 1 × 2 TiN : 1 × 3 × 5	116	1.58
OR-2(Ti) (Ti-termination)	[10$\bar{1}$0] ‖ [110] (1.0%) in hexagonal supercell		[0001] ‖ [111]	$\beta - Si_3N_4$: 2 × 2 × 3 TiN : 5 × 5 × 1	318	3.59
OR-2(N) (N-termination)	[10$\bar{1}$0] ‖ [110] (1.0%) in hexagonal supercell		[0001] ‖ [111]	$\beta - Si_3N_4$: 2 × 2 × 3 TiN : 5 × 5 × 1	318	1.04
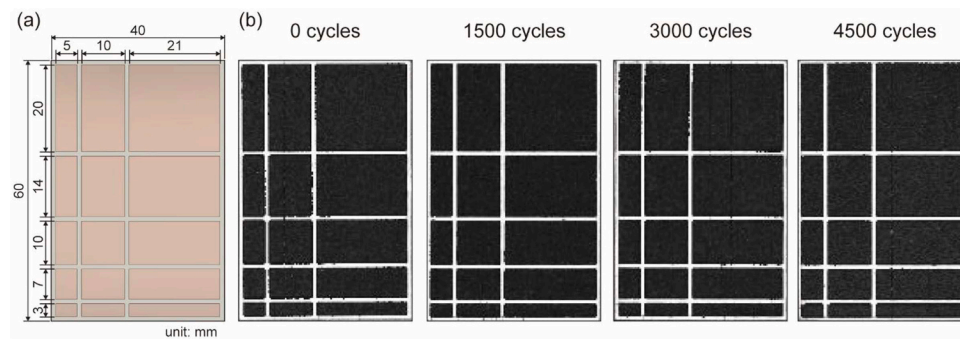
Fig. 9. TCT evaluation of the TiN-intermediated Cu/β-Si$_3$N$_4$/Cu substrate: (a) schematic of the test sample geometry and circuit patterns ranging from 3 × 5 to 20 × 21 mm; (b) representative SAT images acquired at 0, 1500, 3000, and 4500 cycles, where black regions indicate well-bonded areas, demonstrating no significant delamination.

substrates are shown in Fig. 9a. To assess the influence of circuit pattern size on reliability, test patterns ranging from 3 × 5 to 20 × 21 mm were prepared. As shown in the SAT images in Fig. 9b, no significant delamination was observed even after 4500 cycles, with quantitative analysis showing a negligible increase in the delamination ratio of less than 1 %. This demonstrates the excellent interfacial reliability of the TiN-intermediated Cu/β-Si$_3$N$_4$/Cu structure. Furthermore, the influence of circuit pattern size on delamination behavior was minimal. These results confirm that the TiN-intermediated Cu/β-Si$_3$N$_4$/Cu substrates fabricated with a TiN interlayer exhibit high thermal cycling durability, making them suitable for power electronics applications requiring robust reliability under extreme thermal stress.

4. Conclusion

This study investigated the atomistic mechanisms governing the robust bonding between β-Si$_3$N$_4$ and Cu via a Ti-induced TiN interlayer. By integrating PES calculations, TEM observations, and first-principles interface modeling, we demonstrated that Ti exhibits strong interfacial affinity and promotes the formation of structurally coherent and strongly bonded β-Si$_3$N$_4$/TiN interfaces. The identification of five distinct ORs with minimal lattice misfit highlights the structural adaptability of this system. DFT calculations confirmed that these low-misfit ORs yield energetically stable interfaces. As revealed by electronic structure analysis, the high work of adhesion originates from strong covalent–ionic Ti–N bonding. This indicates that the system's robustness arises from its ability to form multiple, structurally coherent, and strongly bonded interfaces. Notably, TCT confirmed the long-term reliability of the TiN-intermediated Cu/β-Si$_3$N$_4$/Cu substrates, with quantitative analysis showing a negligible delamination increase of less than 1 % after 4500 cycles. These findings provide atomistic insight into Ti-mediated metal–ceramic bonding and establish an integrated computational–experimental framework for interface design based on crystallographic matching, adhesion energies, and electronic structure analyses. This work offers both fundamental understanding and practical design guidelines for engineering high-reliability metal–ceramic

interfaces through intermediate compound layers, contributing to the development of next-generation power electronics packaging systems capable of withstanding extreme thermal and mechanical environments.

Data availability

All data generated or analyzed in this study are included in this published article or are available from the corresponding author upon reasonable request.

CRediT authorship contribution statement

Declaration of competing interest

The authors declare that they have no known competing financial interests or personal relationships that could have appeared to influence the work reported in this paper.

Acknowledgments

Appendix A. Detailed computational parameters

All first-principles calculations were performed using the OpenMX (Open source package for Material eXplorer) code package [25,26], which is based on density functional theory (DFT) formulated with a linear combination of atomic orbitals (LCAO). The exchange-correlation potential was described by the Generalized Gradient Approximation (GGA) with the Perdew-Burke-Ernzerhof (PBE) functional [27]. Spin polarization was included in all calculations. The electronic temperature was set to 300 K. Norm-conserving pseudopotentials from the OpenMX Ver. 2019 PBE (PBE19) database were used. The optimized pseudo-atomic orbitals (PAO) basis sets were Si: Si7.0-s2p2d1, N: N6.0-s3p3d2, Ti: Ti7.0-s3p3d2, Ag: Ag7.0-s2p2d2f1, Al: Al7.0-s3p3d2, and Cu: Cu6.0S-s2p2d2. A real-space grid cutoff of 160 Ryd was used. The self-consistent field (SCF) iterations were considered converged when the change in total energy was less than 1.0×10^{-7} Hartree. Geometry optimizations were performed until the maximum force on any atom was below 1.0×10^{-3} Hartree/Bohr. K-point grids were chosen based on total-energy convergence and model dimensionality.

Appendix B. Bonding test and validation of PES predictions

To validate the PES-based deposition material selection, Cu–β-Si$_3$N$_4$ bonding tests were conducted on specimens prepared under different deposition conditions. Ti, Al, and Ag were deposited onto the β-Si$_3$N$_4$ surface before bonding, and an additional set of specimens was bonded without any prior deposition. The detailed bonding procedure corresponds to Section 2.1. After bonding, the specimens were cut into strips with dimensions of 140 mm × 15 mm. The bonding strength of each sample was evaluated using a peeling test.

The peeling test results, shown in Fig. A1, reveal a clear dependence of bonding strength on the deposited material. The Ti-deposited specimens exhibited significantly high bonding strength, consistent with their strong adsorption affinity predicted by the PES calculations. By contrast, the Al- and Ag-deposited specimens, as well as those without deposition, showed significantly lower bonding strength. These experimental findings support the computational results, confirming that Ti provides the highest bonding compatibility with β-Si$_3$N$_4$.
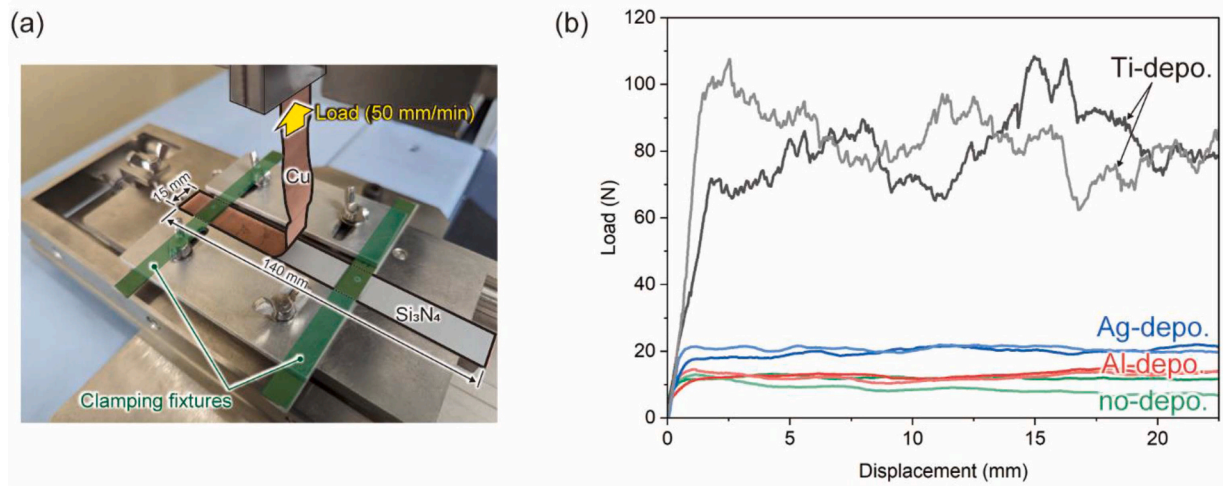

Fig. A1. Peeling test results: (a) test setup and (b) displacement-load curves, where two specimens were tested for each condition: Ti-, Al-, and Ag-deposition, as well as no deposition.

Appendix C. Validation of DFT calculations for bulk and surface properties of β-Si$_3$N$_4$ and TiN

To ensure the reliability of the DFT calculations used to evaluate W_{ad} between β-Si$_3$N$_4$ and TiN, fundamental bulk and surface properties were first examined and compared with previously reported data. The accuracy of the bulk structures was assessed by calculating the relaxed lattice parameters of β-Si$_3$N$_4$ and TiN, as summarized in Table A1. The obtained values showed good agreement with literature data, confirming the validity of the computational setup. In addition, the surface energies of several low-index planes of β-Si$_3$N$_4$ and TiN were calculated to further verify the consistency of the DFT results using the following equation:

$$\gamma_s = \frac{E_{slab} - E_{bulk}}{2A} \tag{A1}$$

where γ_s is the surface energy, E_{slab} is the total energy of the surface slab model, E_{bulk} is the total energy of the corresponding bulk model, and A is the surface area of the slab. In the surface slab model, both the atomic positions and supercell dimensions were relaxed. The calculated γ_s values, listed in Table A2, show reasonable agreement with reported literature values, confirming the suitability of the models employed in this study for evaluating W_{ad}.

Table A1
Calculated lattice parameters of relaxed β-Si$_3$N$_4$ and TiN compared with published data.

System	Structure	Lattice constants (Å)	Reference
β-Si$_3$N$_4$	HCP	$a = 7.70$ $c = 2.94$	This work
		$a = 7.62$ $c = 2.91$	[21]
		$a = 7.65$ $c = 2.93$	[36]
TiN	FCC (rock-salt type)	$a = 4.25$	This work
		$a = 4.24$	[37]
		$a = 4.25$	[38]

Table A2
Calculated surface energies of β-Si$_3$N$_4$ and TiN for selected crystallographic planes compared with literature values.

System	Orientation	γ_s (J/m^2)	Reference
β-Si$_3$N$_4$	(0001)	2.70	This work
		3.05	[21]
		2.68	[39]
	(10$\bar{1}$0)	2.42	This work
		4.17	[21]
		2.47	[39]
	(11$\bar{2}$0)	1.85	This work
		3.93	[21]
		2.89	[39]
TiN	(100)	1.32	This work
		1.26	[40]
	(110)	2.69	This work
		2.64	[40]

References

[1] C. Yang, C. Hu, C. Xiang, H. Nie, X. Gu, L. Xie, J. He, W. Zhang, Z. Yu, J. Luo, Interfacial superstructures and chemical bonding transitions at metal-ceramic interfaces, Sci. Adv. 7 (2021) eabf6667.

[2] G. Mirone, A. Sitta, G. D'Arrigo, M. Calabretta, Material Characterization and Warpage Modeling for Power Devices Active Metal Brazed Substrates, IEEE Trans. Device Mater. Reliab. 19 (2019) 537–542.

[3] M.M. Tousi, M. Ghassemi, Characterization of Nonlinear Field-Dependent Conductivity Layer Coupled With Protruding Substrate to Address High Electric Field Issue Within High-Voltage High-Density Wide Bandgap Power Modules, IEEE J Emerg Sel Top Power Electron 8 (2020) 343–350.

[4] E. Gurpinar, B. Ozpineci, S. Chowdhury, Design, Analysis, Comparison, and Experimental Validation of Insulated Metal Substrates for High-Power Wide-Bandgap Power Modules, J. Electron. Packag. 142 (2020) 041107.

[5] Y. Wang, Y. Ding, Z. Yuan, H. Peng, J. Wu, Y. Yin, T. Han, F. Luo, Space-Charge Accumulation and Its Impact on High-Voltage Power Module Partial Discharge Under DC and PWM Waves: testing and Modeling, IEEE Trans. Power Electron. 36 (2021) 11097–11108.

[6] H.M. Lee, E.B. Lee, D.L. Kim, D.K. Kim, Comparative study of oxide and non-oxide additives in high thermal conductive and high strength Si$_3$N$_4$ ceramics, Ceram. Int. 42 (2016) 17466–17471.

[7] T. Lu, T. Wang, Y. Jia, M. Ding, Y. Shi, J. Xie, F. Lei, L. Zhang, L. Fan, Fabrication of high thermal conductivity silicon nitride ceramics by pressureless sintering with MgO and Y2O3 as sintering additives, Ceram. Int. 46 (2020) 27175–27183.

[8] A. Fukumoto, D. Berry, K.D.T. Ngo, G.-Q. Lu, Effects of Extreme Temperature Swings (-55 °C to 250 °C) on Silicon Nitride Active Metal Brazing Substrates, IEEE Trans. Device Mater. Reliab. 14 (2014) 751–756.

[9] G. Böhm, D. Brunner, I. Sichert, A. Pönicke, J. Schilm, Properties and Reliability of Silicon Nitride Substrates With AMB Copper Conductor, IMAPS - International Microelectronics Assembly and Packaging Society, 2011, pp. 000777–000784.

[10] Y. Mori, S. Fujisawa, K. Morimoto, M. Yonei, H. Kato, S. Suenaga, Development of Ag-free active metal brazing filler for manufacturing copper-Si$_3$N$_4$ substrates, in: PCIM Europe 2023; International Exhibition and Conference for Power Electronics, Intelligent Motion, Renewable Energy and Energy Management, ieeexplore.ieee.org, 2023, pp. 1–6.

[11] M.C. Ngo, H. Miyazaki, K. Hirao, T. Ohji, M. Fukushima, Stress–strain behavior of Cu on the AMB-Si$_3$N$_4$ substrate undergoing thermal cycles via in situ strain measurement, J. Am. Ceram. Soc. 107 (2024) 8415–8425.

[12] S. Yang, J. Wu, A. Christou, Initial stage of silver electrochemical migration degradation, Microelectron. Reliab. 46 (2006) 1915–1921.

[13] Y. Song, H. Zhu, D. Liu, X. Song, C. Tan, J. Cao, Direct bonding of silicon nitride to copper via laser surface modification, Appl. Surf. Sci. 602 (2022) 154354.

[14] Y. Song, D. Liu, G. Jin, H. Zhu, N. Chen, S. Hu, X. Song, J. Cao, Fabrication of Si$_3$N$_4$/Cu direct-bonded heterogeneous interface assisted by laser irradiation, J. Mater. Sci. Technol. 99 (2022) 169–177.

[15] Y. Song, L. Liu, D. Liu, X. Song, J. Cao, Low-temperature bonding of Cu on Si$_3$N$_4$ substrate by using Ti/Cu thin films, Mater. Lett. 320 (2022) 132330.

[16] G. Liu, D. Wang, Y. Xing, X. Zhong, W. Pan, Copper bonding silicon nitride substrate using atmosphere plasma spray, J. Eur. Ceram. Soc. 43 (2023) 3981–3987.

[17] C. Xin, R. Yuan, J. Wu, Q. Wang, Y. Zhou, Fabrication and joining mechanism of Nano-Cu/Si$_3$N$_4$ ceramic substrates, Ceram. Int. 47 (2021) 3411–3420.

[18] H. Tatsumi, S. Moon, M. Takahashi, T. Kozawa, E. Tsushima, H. Nishikawa, Quasi-direct Cu–Si$_3$N$_4$ bonding using multi-layered active metal deposition for power-module substrate, Mater. Des. 238 (2024) 112637.

[19] T. Shimoo, K. Okamura, S. Adachi, Interaction of Si$_3$N$_4$ with titanium at elevated temperatures, J. Mater. Sci. 32 (1997) 3031–3036.

[20] C. Iwamoto, S.-I. Tanaka, Interface nanostructure of brazed silicon nitride, J. Am. Ceram. Soc. 81 (1998) 363–368.

[21] S. Yang, B. Yang, H. Ren, H. Yang, X. Pang, K. Gao, A.A. Volinsky, Selection of interfacial metals for Si$_3$N$_4$ ceramics by the density functional theory, Chem. Phys. Lett. 763 (2021) 138189.

[22] X. Gui, M. Zhang, P. Xu, G. Liu, Q. Guo, X. Zhang, H. Meng, G. Qiao, Experimental and theoretical study on air reaction wetting and brazing of Si$_3$N$_4$ ceramic by Ag-CuO filler metal: performance and interfacial behavior, J. Eur. Ceram. Soc. 42 (2022) 432–441.

[23] Z. Xiangzhao, Z. Yansheng, Z. Yinuo, C. Kerou, L. Guiwu, Q. Guanjun, Theoretical screening and experimental fabrication of metallized layer for enhanced Cu wetting and adhesion on Si$_3$N$_4$ substrate, Ceram. Int. 51 (2025) 12940–12950.

[24] H.-Y. Kwon, Z. Morrow, C.T. Kelley, E. Jakubikova, Interpolation methods for molecular potential energy surface construction, J. Phys. Chem. A 125 (2021) 9725–9735.

[25] T. Ozaki, Variationally optimized atomic orbitals for large-scale electronic structures, Phys. Rev. B 67 (2003) 155108.

[26] T. Ozaki, H. Kino, Numerical atomic basis orbitals from H to Kr, Phys. Rev. B (2004), https://doi.org/10.1103/PhysRevB.69.195113.

[27] J.P. Perdew, K. Burke, M. Ernzerhof, Generalized gradient approximation made simple, Phys. Rev. Lett. 77 (1996) 3865–3868.

[28] B. Morrison, Kleinman, Nonlocal Hermitian norm-conserving Vanderbilt pseudopotential, Phys. Rev., B Condens. Matter 47 (1993) 6728–6731.

[29] K. Lejaeghere, G. Bihlmayer, T. Björkman, P. Blaha, S. Blügel, V. Blum, D. Caliste, I. E. Castelli, S.J. Clark, A. Dal Corso, S. de Gironcoli, T. Deutsch, J.K. Dewhurst, I. Di Marco, C. Draxl, M. Dułak, O. Eriksson, J.A. Flores-Livas, K.F. Garrity, L. Genovese, P. Giannozzi, M. Giantomassi, S. Goedecker, X. Gonze, O. Grånäs, E.K.U. Gross, A. Gulans, F. Gygi, D.R. Hamann, P.J. Hasnip, N.A.W. Holzwarth, D. Iuşan, D. B. Jochym, F. Jollet, D. Jones, G. Kresse, K. Koepernik, E. Küçükbenli, Y. O. Kvashnin, I.L.M. Locht, S. Lubeck, M. Marsman, N. Marzari, U. Nitzsche, L. Nordström, T. Ozaki, L. Paulatto, C.J. Pickard, W. Poelmans, M.I.J. Probert, K. Refson, M. Richter, G.-M. Rignanese, S. Saha, M. Scheffler, M. Schlipf, K. Schwarz, S. Sharma, F. Tavazza, P. Thunström, A. Tkatchenko, M. Torrent, D. Vanderbilt, M.J. van Setten, V. Van Speybroeck, J.M. Wills, J.R. Yates, G.-X. Zhang, S. Cottenier, Reproducibility in density functional theory calculations of solids, Science 351 (2016) aad3000.

[30] M. Otani, O. Sugino, First-principles calculations of charged surfaces and interfaces: a plane-wave nonrepeated slab approach, Phys. Rev. B Condens. Matter Mater. Phys. 73 (2006) 115407.

[31] T. Ohwaki, M. Otani, T. Ikeshoji, T. Ozaki, Large-scale first-principles molecular dynamics for electrochemical systems with O(N) methods, J. Chem. Phys. 136 (2012) 134101.

[32] H. Miyazaki, Y. Zhou, S. Iwakiri, H. Hirotsuru, K. Hirao, S. Fukuda, N. Izu, H. Hyuga, Improved resistance to thermal fatigue of active metal brazing substrates for silicon carbide power modules using tough silicon nitrides with high thermal conductivity, Ceram. Int. 44 (2018) 8870–8876.

[33] H. Yang, B. Zeng, H. Wang, H. Jin, C. Zhou, Phase equilibria and thermodynamic re-assessment of the Cu–Ti system, CALPHAD 82 (2023) 102594.

[34] B.L. Bramfitt, The effect of carbide and nitride additions on the heterogeneous nucleation behavior of liquid iron, Metall. Trans. 1 (1970) 1987–1995.

[35] A. Forslund, X. Zhang, B. Grabowski, A.V. Shapeev, A.V. Ruban, Ab initio simulations of the surface free energy of TiN(001), Phys. Rev. B. 103 (2021), https://doi.org/10.1103/physrevb.103.195428.

[36] M. Yang, R.Q. Wu, W.S. Deng, L. Shen, Z.D. Sha, Y.Q. Cai, Y.P. Feng, S.J. Wang, Electronic structures of β-Si$_3$N$_4$(0001)/Si(111) interfaces: perfect bonding and dangling bond effects, J. Appl. Phys. 105 (2009) 024108.

[37] L. Rao, H. Liu, S. Liu, Z. Shi, X. Ren, Y. Zhou, Q. Yang, Interface relationship between TiN and Ti substrate by first-principles calculation, Comput. Mater. Sci. 155 (2018) 36–47.

[38] X. Fan, B. Chen, M. Zhang, D. Li, Z. Liu, C. Xiao, First-principles calculations on bonding characteristic and electronic property of TiC (111)/TiN (111) interface, Mater. Des. 112 (2016) 282–289.

[39] S.X. Tao, A. Theulings, J. Smedley, H. van der Graaf, DFT study of electron affinity of hydrogen terminated β-Si$_3$N$_4$, Diam. Relat. Mater. 53 (2015) 52–57.

[40] M. Gsellmann, D. Scheiber, T. Klünsner, J. Zálešák, Z. Zhang, H. Leitner, C. Mitterer, G. Ressel, L. Romaner, Bond strength between TiN coating and microstructural constituents of a high speed steel determined by first principle calculations, Acta Mater. 222 (2022) 117439.